J. Fluid Mech. (2013), *vol.* 719, *pp.* 406–430.
doi:10.1017/jfm.2012.610

Stochastic dynamics and model reduction of amplifier flows: the backward facing step flow

G. Dergham[1,2], D. Sipp[2] and J.-Ch. Robinet[1,†]

[1]DynFluid Laboratory, Arts et Métiers ParisTech, 151 Boulevard de l'Hôpital, 75013 Paris, France
[2]ONERA, The French-Aerospace Lab, 8 rue des Vertugadins, 92190 Meudon, France

(Received 9 January 2012; revised 10 October 2012; accepted 7 December 2012)

Methods for investigating and approximating the linear dynamics of amplifier flows are examined in this paper. The procedures are derived for incompressible flow over a two-dimensional backward-facing step. First, the singular value decomposition of the resolvent is performed over a frequency range in order to identify the optimal and suboptimal harmonic forcing and responses of the flow. These forcing/responses are shown to be organized into two categories: the first accounting for the Orr and Kelvin–Helmholtz instabilities in the shear layer and the second for the advection and diffusion of perturbations in the free stream. Next, we investigate the dynamics of the flow when excited by a white in space and time noise. We compute the predominant patterns of the random flow which optimally account for the sustained variance, the empirical orthogonal functions (EOFs), as well as the predominant forcing structures which optimally contribute to the sustained variance, the stochastic optimals (SOs). The leading EOFs and SOs are expressed as a linear combination of the suboptimal forcing and responses of the flow and are related to particular instability mechanisms and/or frequency intervals. Finally, we use the leading EOFs, SOs and balanced modes (obtained from balanced truncation) to build low-order models of the flow dynamics. These models are shown to accurately recover the time propagator and resolvent of the original dynamical system. In other words, such models capture the entire flow response from any forcing and may be used in the design of efficient closed-loop controllers for amplifier flows.

Key words: flow control, instability

1. Introduction

A typical feature of a wide variety of open flows is their unstable nature and high sensitivity to background perturbations. This behaviour is classically observed in boundary layers, mixing layers, jets or separated flows, even at low Reynolds numbers. Such a behaviour is related to convective instabilities which amplify disturbances while being advected downstream. These flows are called selective noise amplifiers owing to their ability to preferentially amplify some particular frequency ranges.

The linear dynamics in noise amplifiers may be complex and involves different physical mechanisms such as convective instabilities of various physical origins

† Email address for correspondence: Jean-christophe.ROBINET@ensam.eu

(Kelvin–Helmholtz, Tollmien–Schlichting, Orr, etc.), advection and diffusion. These mechanisms are usually characterized either in the time or frequency domain. For instance, considering a small perturbation $\boldsymbol{x}(t)$ around a given base flow, the linear dynamics of the flow is governed by an equation of the form

$$\dot{\boldsymbol{x}} = \boldsymbol{A}\,\boldsymbol{x} + \boldsymbol{f}(t) \tag{1.1a}$$

where the dynamical operator $\boldsymbol{A}$ is stable and where the dynamics is driven by the external forcing $\boldsymbol{f}(t)$ which stands for noise or an actuation. On the one hand, the amplifier behaviour may be assessed by looking for the disturbance which leads to the maximum energy growth, the so-called optimal perturbation, and follow the evolution of this perturbation, see Blackburn, Barkley & Sherwin (2008) and Marquet *et al.* (2008). In this approach, the optimal initial perturbation for a time horizon t and the optimal perturbation into which it evolves may be found as the leading singular vectors of the time propagator $\mathrm{e}^{\boldsymbol{A}t}$, see Trefethen *et al.* (1993) and Farrell & Ioannou (1996). Alternatively, another option consists of finding the external harmonic forcing of frequency ω which yields the most energetic flow response, see Åkervik *et al.* (2008), Alizard, Cherubini & Robinet (2009), Monokrousos *et al.* (2010) and Sipp *et al.* (2010). Similarly, the optimal forcing and its associated response may be found as the leading singular vectors of the resolvent operator $\boldsymbol{R}(\omega) = (\mathrm{i}\omega\boldsymbol{I} - \boldsymbol{A})^{-1}$. Both the time- and frequency-based approaches highlight the most energetic instability mechanisms at play. However, none of the previous studies in the literature has examined the link between the other leading singular vectors of $\mathrm{e}^{\boldsymbol{A}t}$ or $\boldsymbol{R}(\omega)$, also referred to as suboptimal perturbations, and the dynamics of the flow. In this context, the objective of this paper is twofold.

First, realistic flow configurations are always subject to complex noise excitations which are not predictable, such as residual turbulence, acoustic disturbances or geometric defects. One important question is to investigate if the optimal perturbations or optimal forcing responses may be observed in a case where the flow is continuously forced by a random forcing. In this context, one may consider a stochastic forcing $\boldsymbol{f}(t)$ in the equations, characterized by its probability properties, see Farrell & Ioannou (1993*a*). The random noise is regarded as an input and the resulting random flow field $\boldsymbol{x}(t)$ as an output. As a result, the ability of the flow to amplify perturbations can be assessed by examining the ratio of the output variance to that of the input. The input is usually chosen as a white in space and time noise forcing so as to mimic in an unbiased manner real noise. The idea is then to look for the flow structures $\boldsymbol{x}(t)$ which optimally account for the system sustained variance. These modes are known as proper orthogonal decomposition (POD) modes or also empirical orthogonal functions (EOFs) and constitute energy-ranked coherent structures of the uncertain flow, see North (1984) in the context of climate modelling and Berkooz, Holmes & Lumley (1993) in turbulence modelling. In a similar manner, one may determine the set of uncorrelated coherent forcing terms $\boldsymbol{f}(t)$ ranked by their contribution to the evolved flow state sustained variance. These are referred to as stochastic optimals (SOs), see Farrell & Ioannou (1993*a*,*b*, 2001). The stochastic forcing approach has been successfully applied in systems with a small number of degrees of freedom by Fontane, Brancher & Fabre (2008). Our goal is to show how these quantities may be computed for high dimensional fluid systems and how these structures (EOFs and SOs) may be related to the instabilities displayed by the system (optimal perturbations or optimal forcing responses). Notably, the relation between the flow instabilities and the most probable coherent structures arising from the stochastic forcing is an important issue.

Second, this work is also motivated by the model reduction of high-dimensional fluid systems. Reduced-order models (ROMs) of the dynamics are important in three respects. (i) A better understanding of the physical phenomena may be obtained by determining ROMs of the flow, which put into light the fundamental mechanisms at play with the fewest possible degrees of freedom. For example, amplitude equations which govern the dynamics of global modes in systems undergoing bifurcations are examples of such an approach. Obtaining the smallest possible ROM which recovers accurately the dynamics from all inputs to all outputs from a Galerkin projection may yield relevant information on the underlying flow physics: for example, the leading structures of the primal and dual projection bases precisely indicate regions of interest of the flow. (ii) Accurate ROMs are valuable tools for extensive parametric studies: here we aim at building models that capture the whole input and output spaces with the fewest degrees of freedom. These models are therefore fully equivalent to costly high-dimensional direct numerical simulations (DNSs). (iii) Finally, real-time closed-loop control of noise-amplifier flows requires knowledge of an accurate model of the flow dynamics of small dimension. For example, the recent work by Bagheri, Brandt & Henningson (2009) relies on a ROM which captures the linear dynamics between some inputs (an actuator and a 'known' noise source) to some outputs (two sensors) in view of performing a closed-loop control of a spatially developing boundary layer. The authors successfully stabilized the flow by using an efficient low-order linear quadratic Gaussian (LQG) compensator, which was designed to minimize the measurement energy of a given sensor. Now, it would be of great technological interest to have a model which could accurately recover the entire flow response (all of the outputs) from all possible forcing (all of the inputs). Such an improvement would allow us to capture both the effect of any unspecified noise, as it would be in real experiments, and also to directly target the global perturbation kinetic energy rather than some specific measurement. How to design low-order dynamical systems capturing the dynamics between all inputs to all outputs and how to relate the projection bases used in the process to optimal perturbations or optimal forcing responses precisely constitutes the second motivation of this paper.

The EOFs and SOs are defined as the leading eigenvectors of the covariance matrix $\boldsymbol{P} = \int_0^{+\infty} \mathrm{e}^{\boldsymbol{A}t}\mathrm{e}^{\boldsymbol{A}^\dagger t}\,\mathrm{d}t$ and of the matrix $\boldsymbol{Q} = \int_0^{+\infty} \mathrm{e}^{\boldsymbol{A}^\dagger t}\mathrm{e}^{\boldsymbol{A}t}\,\mathrm{d}t$ respectively, see Farrell & Ioannou (1993*a*). Regarding model reduction, we will consider Galerkin models obtained by projection of the linearized Navier–Stokes equations on three different bases: the EOFs, which also correspond to the most controllable modes; the SOs, which also correspond to the most observable modes; and the balanced modes. Moore (1981) showed that the latter modes correspond to the eigenvectors of $\boldsymbol{PQ}$ and that they quasi-optimally capture the input–output dynamics. For systems of small size, having up to $O(10^3)$ degrees of freedom, all of these modes can be obtained by solving directly the related eigenproblem. However, their computation becomes untractable for larger systems. The approach considered in this paper is to approximate the leading eigenvectors of $\boldsymbol{P}$, $\boldsymbol{Q}$ and $\boldsymbol{PQ}$ by building accurate low-rank approximations of these matrices, based on optimal forcing/response. Once the low-rank approximations of $\boldsymbol{P}$ and $\boldsymbol{Q}$ have been established, the treatment to obtain the various modes follows the classical algorithms given by Laub *et al.* (1987) and Rowley (2005). It should be mentioned that the present technique goes beyond the output projection technique (Rowley 2005), which captures the whole output space but only few inputs, and beyond the input projection technique (Dergham, Sipp & Robinet 2011), which captures the whole input space but only few outputs.

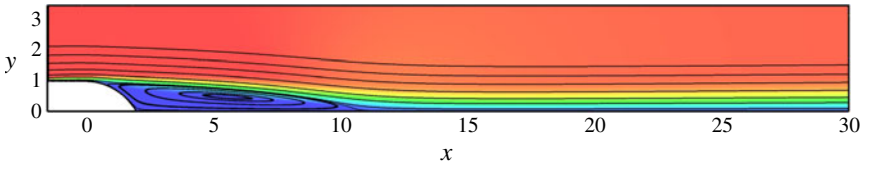

FIGURE 1. Backward-facing step flow investigated in this paper. The steady-state solution at $Re = 600$ is depicted by its streamlines and longitudinal velocity.

The present analysis is illustrated on a canonical amplifier flow, the case of an incompressible two-dimensional backward-facing step flow. The flow displays an elongated recirculation bubble for a Reynolds number $Re = 600$ based on the step height. Perturbations are shown to be amplified in the shear layer owing to the Kelvin–Helmholtz and Orr instabilities while they are purely advected and diffused in the free stream. Blackburn *et al.* (2008) have investigated the response of such a flow to upstream random forcing. In particular, they showed how the optimal initial perturbations may shed some new light on the observed dynamics. Here, in the spirit of the works by Alizard *et al.* (2009) and Sipp & Marquet (2012), we switch to the frequency space and determine the optimal forcings/responses. We will analyse how the various physical mechanisms mentioned above are represented by such structures. We will, in particular, discuss the advection–diffusion phenomenon in the free stream, which is usually linked to the continuous spectrum (Grosch & Salwen 1978). Also, we will highlight the link between the leading EOFs/SOs and the instability mechanisms, i.e. the optimal forcing/response.

The paper is organized along the following outline: the backward-facing step flow is presented in § 2, where we also present the base flow and the equations governing the linear dynamics. Section 3 is devoted to the decomposition in the frequency domain of the input–output dynamics. In particular, the optimal harmonic forcing/response of the flow are investigated. Next, the leading EOFs and SOs are computed and discussed (§ 4). The question of model reduction is addressed in § 5. After introducing the balanced modes, the ability of the ROMs obtained by Galerkin projection to capture the original dynamics is assessed for all three bases. Finally, concluding remarks and future prospects are given in § 6.

2. Flow configuration and modelling

2.1. *Base flow*

We consider the dynamics of the incompressible flow over a two-dimensional backward-facing step (see figure 1). It is made up with two flat plates linked by a circular arc extending from $(x = 0,\ y = 1)$ to $(x = 2,\ y = 0)$. The step height h and the incoming flow velocity U_∞ are chosen as the characteristic length and velocity scales so that the Reynolds number is defined by $Re = U_\infty h/\nu$ where ν is the kinematic viscosity.

The flow dynamics is linearized about a base flow chosen as the steady solution of the Navier–Stokes equations at $Re = 600$. To compute the base flow, the domain is chosen large enough so as to obtain a uniform free stream. The flow enters the domain with the constant velocity $(u = 1, v = 0)$ from the left at $x = -20$. We imposed a free-slip condition $(\partial_y u = 0, v = 0)$ on the upstream part of the lower boundary $(-20 \leqslant x \leqslant -2, y = 1)$. The beginning of a laminar boundary layer is then

enforced at $x = -2$ by imposing a no-slip condition ($u = 0, v = 0$) on the remaining lower boundary between ($-2 \leqslant x \leqslant 100$). A symmetry condition ($\partial_y u = 0, v = 0$) is implemented on the top boundary at $y = 20$ and a standard outflow condition is prescribed at the outlet $x = 100$. The base flow is computed by using a Newton method similar to that used by Sipp *et al.* (2010).

The base flow solution at $Re = 600$ is depicted in figure 1 by its streamlines and longitudinal velocity. The flow displays an elongated recirculation bubble between separation at $x \approx 0.6$ and reattachment at $x \approx 11$. The boundary layer at $x = 0$ has a displacement thickness $\delta^* = 0.082$ leading to a Reynolds number based on the displacement thickness of $Re_{\delta^*} = 49.2$.

2.2. *Linear dynamics*

The dynamics of small perturbations $(\boldsymbol{u}, p)$ about the base flow, denoted by $\boldsymbol{U}$, are governed by the linearized Navier–Stokes equations

$$\partial_t \boldsymbol{u} + \boldsymbol{U} \cdot \boldsymbol{\nabla} \boldsymbol{u} + \boldsymbol{u} \cdot \boldsymbol{\nabla} \boldsymbol{U} = -\boldsymbol{\nabla} p + Re^{-1} \nabla^2 \boldsymbol{u} + f(t), \quad \boldsymbol{\nabla} \cdot \boldsymbol{u} = 0 \tag{2.1}$$

where we have introduced a forcing term $f(t)$ on the momentum equation. We focus on the dynamics of perturbations in a smaller domain extending from ($-1.5 \leqslant x \leqslant 30$) and ($y \leqslant 3.5$). This domain, depicted in figure 1, is sufficiently large to accurately capture the perturbation dynamics along the shear layer. Homogeneous Dirichlet boundary conditions ($u = 0, v = 0$) are used at the inflow $x = -1.5$ and on the wall, a symmetry condition ($\partial_y u = 0, v = 0$) is adopted at the upper boundary $y = 3.5$ and a free outflow condition $p\boldsymbol{n} - Re^{-1}(\boldsymbol{\nabla} \boldsymbol{u}) \cdot \boldsymbol{n} = 0$ is used at the outlet $x = 30$, where $\boldsymbol{n}$ is the outward unit normal vector. Note that the base flow corresponds to that computed in the large domain which has been interpolated on a smaller mesh. This system is spatially discretized using a finite elements approach with Taylor–Hood elements (P2–P2–P1) and implemented using the FreeFem++ software, see Hecht *et al.* (2005). Once discretized, (2.1) can be written in the form

$$\dot{\boldsymbol{x}} = \boldsymbol{A}\boldsymbol{x} + \boldsymbol{f}(t) \tag{2.2}$$

where $\boldsymbol{x}$ is the vector of the discretized velocities $\boldsymbol{u}$, $\boldsymbol{A}$ the discretized Navier–Stokes operator and $\boldsymbol{f}(t)$ the discretized forcing term. The number of degrees of freedom of the resulting problem is $n = 170\,260$, which also accounts for the dimension of the vector $\boldsymbol{x}$ and of the matrix $\boldsymbol{A}$ in (2.2).

For the chosen Reynolds number $Re = 600$, the flow is observed to be globally stable since the matrix $\boldsymbol{A}$ does not display any unstable eigenvalues. It has also been checked that the flow remains globally stable for Reynolds numbers up to 2000, showing that the present configuration is far from any global instability mechanism. However, perturbations may be transiently amplified owing to the non-normality of $\boldsymbol{A}$, see Chomaz (2005). In this case, the dynamics of the flow is assessed by its ability to amplify external disturbances, such as the forcing $\boldsymbol{f}(t)$. The amplitude of perturbations is quantified in the following by its kinetic energy integrated in the entire domain. To this end, we introduce the inner product $\langle\,\rangle$ defined for any states $\boldsymbol{x}_1$ and $\boldsymbol{x}_2$ by

$$\langle \boldsymbol{x}_1, \boldsymbol{x}_2 \rangle = \boldsymbol{x}_1^\dagger \boldsymbol{x}_2 = \int_\Omega \boldsymbol{u}_1 . \boldsymbol{u}_2 \, \mathrm{d}\Omega \tag{2.3}$$

where Ω is the fluid volume, $\boldsymbol{u}_1$ and $\boldsymbol{u}_2$ denote the associated velocity fields and the superscript † denotes the adjoint of a state.

3. Dynamics decomposition in the frequency domain

Studying the responses of a flow subjected to harmonic forcing is known as a receptivity analysis. Such an approach is commonly used to predict in which frequency bands flow instabilities are more likely to be observed when exposed to permanent external forcing, see Alizard *et al.* (2009), Monokrousos *et al.* (2010) and Sipp *et al.* (2010). In this section, we compute the leading optimal forcing and response over a frequency range in order to identify the predominant physical mechanisms at play. Mostly, we wish to decompose the input–output dynamics in the frequency domain in view of computing the leading EOFs/SOs and balanced modes.

3.1. *Singular value decomposition of the resolvent*

Assuming that system (2.2) is forced by the harmonic term $\boldsymbol{f}(t) = \hat{\boldsymbol{f}}\mathrm{e}^{\mathrm{i}\omega t}$, a solution is sought in the form $\boldsymbol{x}(t) = \hat{\boldsymbol{x}}\mathrm{e}^{\mathrm{i}\omega t}$: $\hat{\boldsymbol{x}}(\omega) = \boldsymbol{R}(\omega)\hat{\boldsymbol{f}}$, where the operator $\boldsymbol{R}(\omega) = (\mathrm{i}\omega\boldsymbol{I} - \boldsymbol{A})^{-1}$ is defined as the resolvent and links the harmonic forcing to its associated response. The strongest energy gains are obtained by solving the eigenvalues of

$$\boldsymbol{R}^{\dagger}(\omega)\boldsymbol{R}(\omega)\hat{\boldsymbol{f}}_i = \lambda_i^2\hat{\boldsymbol{f}}_i \tag{3.1}$$

where $\boldsymbol{R}^{\dagger}(\omega)$ is the adjoint operator derived from the inner product $\langle\,\rangle$. Here λ_i^2 denote the energy gains induced by the forcing $\hat{\boldsymbol{f}}_i$. The highest eigenvalue λ_1^2 denotes the maximum energy gain over all possible forcing, which is reached by the optimal forcing $\hat{\boldsymbol{f}}_1$. Their corresponding optimal responses $\hat{\boldsymbol{x}}_i$ can be obtained by solving

$$\hat{\boldsymbol{x}}_i = \boldsymbol{R}(\omega)\hat{\boldsymbol{f}}_i \tag{3.2}$$

which also form an orthogonal basis spanning the response space. In fact, $\hat{\boldsymbol{f}}_i(\omega)$ and $\hat{\boldsymbol{x}}_i(\omega)$ are the right and left singular vectors of $\boldsymbol{R}(\omega)$ associated with its singular values λ_i.

An iterative Lanczos algorithm is used in order to compute the leading eigenvalues/eigenvectors. It is based on the successive inversion of the sparse matrix $(\mathrm{i}\omega\boldsymbol{I} - \boldsymbol{A})$ which is handled through a direct multifrontal sparse LU solver. Hence, the cost of this algorithm stems from the cost of the LU decomposition of a large sparse complex matrix. Technical details are given by Sipp & Marquet (2012). In our case, an accurate computation of the leading 40 eigenvalues/eigenvectors has been performed for frequencies ranging from $\omega = 0$ to $\omega = 6$. For a given frequency, one eigenvalue problem lasts about 20 min when eight processors are used. The optimal energy gains λ_i^2 are represented in figure 2 as a function of the frequency. In other words, there are 40 points represented on the graph for each frequency which account for $\lambda_1^2, \ldots, \lambda_{40}^2$. The figure clearly displays branches, one of them displaying a broad and high peak. The description of these branches and their physical interpretation is presented next.

3.2. *First branch: the shear layer dynamics*

The higher curved branch denoted on the graph as branch $A1$ is considered first. This branch comprises the first singular value λ_1 which largely prevails for low frequencies until $\omega \approx 2.6$. The energy gain λ_1^2 displays strong values over a large frequency band, which is typical of amplifier flows. A maximum of 2.2×10^6 is reached at $\omega \approx 0.75$. For higher frequencies, branch $A1$ crosses other branches and is then no longer represented by the first singular value.

A physical interpretation of branch $A1$ comes from the forcing and responses associated with its singular values. Branch A1 is associated with amplification of perturbations resulting from shear instabilities. In figure 3 the real part of these

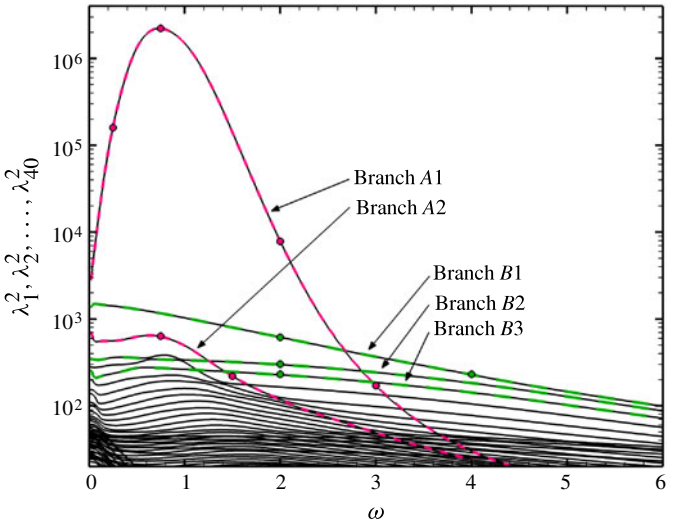

FIGURE 2. First 40 optimal harmonic gains $\lambda_1^2, \ldots, \lambda_{40}^2$ versus frequency ω. Circles denote the singular values that are looked at in more detail.

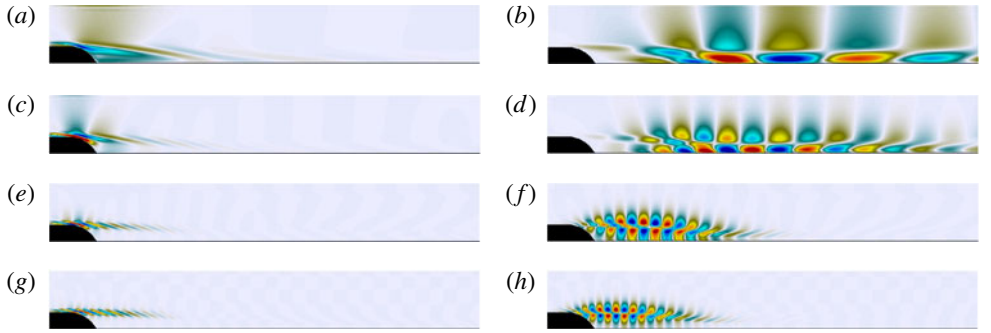

FIGURE 3. Real part of the streamwise velocity of four optimal forcing/responses computed on branch $A1$ for $\omega = 0.25$ (a,b), $\omega = 0.75$ (c,d), $\omega = 2$ (e,f) and $\omega = 3$ (g,h).

singular vectors are represented. On the left part, figure 3(a,c,e,g) represents the optimal harmonic forcing at the frequencies $\omega = 0.25, 0.75, 2$ and 3 respectively. Analogously, figure 3(b,d,f,h) shows the associated optimal harmonic responses at the same frequencies. Note that these flow structures are displayed by their longitudinal velocity. We observe that the optimal forcing fields are localized upstream, near separation, and display inclined patterns along the shear so as to exploit the Orr mechanism. Regarding the associated responses, they display typical wave packet flow structures whose spatial support extends farther downstream. Excitation at higher frequencies leads to smaller flow structures and the resulting responses remain spatially localized at the upstream part of the separated shear layer. In contrast, for lower frequencies, the resulting flow structures are much larger and the responses extend much farther until the downstream part of the boundary layer. High-frequency responses, such as those depicted in figure 3(f,h), highlight a Kelvin–Helmholtz amplification mechanism since perturbations grow in the shear layer as a wave of

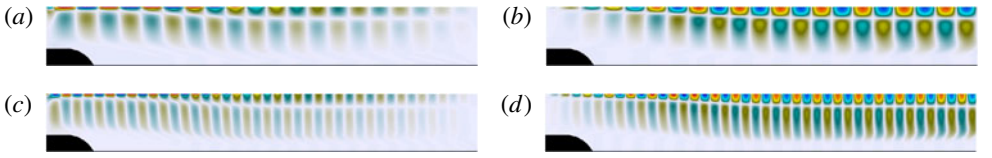

FIGURE 4. Real part of the longitudinal velocity of two optimal forcing/responses computed on branch $B1$ for $\omega = 2$ (a,b) and $\omega = 4$ (c,d).

corotative rolls. These flow structures are furthermore characterized by a phase speed of about $v_\phi \approx 0.55$. Alternatively, the low-frequency responses such as those depicted in figure 3(b,d) are reminiscent of the global modes associated with a convective Tollmien–Schlichting instability. Such modes have been carefully investigated in the previous works by Ehrenstein & Gallaire (2005), Alizard & Robinet (2007) and Åkervik *et al.* (2008) and their phase speed is rather close to $v_\phi \approx 0.4$.

All of the optimal forcing and responses on branch $A1$ have a common point, they physically account for the amplification and advection of a wave packet along the recirculation bubble and the downstream shear. Thus, this branch may be called a 'shear layer' branch.

3.3. *Second branch: the free stream dynamics*

The second most energetic branch which is called $B1$ in figure 2 is now described. Branch B_1 corresponds to advection and diffusion in the free stream, and no amplification mechanism is involved there. In fact, one should not associate the large values of the gain obtained for the B branches to any instability mechanism. Although their gains are important, the B branches are not very energetic. This issue has been thoroughly discussed by Sipp & Marquet (2012). Beyond $\omega \approx 2.6$, branch $A1$ is observed to be no more predominant and the associated energy gains are much lower. The first singular values λ_1^2 then belong to branch $B1$. To further interpret the contribution of this branch to the flow dynamics, two forcing and response fields obtained on that branch are represented in figure 4. Figure 4(a,c) represent the optimal forcing at the frequencies $\omega = 2$ and 4, respectively, while figure 4(b,d) account for the associated optimal responses. Similarly to the previous branch, the forcing fields are located upstream whereas the responses extend downstream. However, both the forcing and the response reduce here to streamwise oscillating waves spreading over the free stream part of the flow. These waves are modulated in the y direction and have two maxima. The only difference between these modes when changing the frequency is the streamwise wavelength of the flow structures. Increasing the frequency leads to a smaller streamwise wavelength for both the forcing and responses. Interestingly, their phase velocity is observed to be constant with the frequency and close to $v_\phi \approx 1$ and correspond to the free stream advection of perturbations. This branch is thus called a 'convective' branch.

3.4. *Other branches: suboptimal modes*

The other branches can also be classified as related to the convection or associated with the shear layer. As an illustrative example, in figure 5(a,b) the two harmonic responses taken from the branches labelled $B2$ and $B3$, respectively, at the frequency $\omega = 2$ are depicted. These responses are very similar to those observed on branch $B1$ except that they display smaller cross-stream wavelengths. More precisely, the

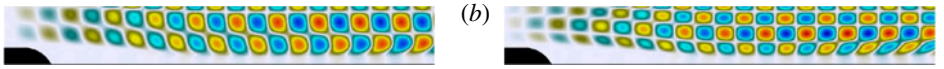

FIGURE 5. Real part of the longitudinal velocity of two optimal responses. (*a*) Response computed at $\omega = 2$ on branch $B2$. (*b*) Response computed at the same frequency on branch $B3$.

FIGURE 6. Real part of the longitudinal velocity of two optimal responses computed on branch $A2$ for (*a*) $\omega = 0.75$ and (*b*) $\omega = 1.5$.

response chosen on $B2$ displays three maxima in the y direction while that on $B3$ has four. These results are reminiscent of the fact that the optimal responses are orthogonal. Generally speaking, the convective branches are meant to convect all possible upstream forcing. The decomposition in such branches then highlights the contribution of all possible streamwise and cross-stream modulated forcing individually.

In an analogous way, we have represented in figure 6 the optimal responses taken on the shear layer branch $A2$ and computed for $\omega = 0.75$ and 1.5, respectively. Both display two streamwise separated wave packets localized in the shear layer. In addition, their streamwise wavelengths are the same as those of the responses observed on branch $A1$ at the same frequencies. This latter observation is also reminiscent of the orthogonality of the set of optimal responses. This second shear layer branch is much less energetic than the primary one and is even less than the first convective branch.

The frequency decomposition discussed in this section has emphasized a clear separation between (i) upstream forcing and downstream responses, but mostly (ii) a free stream convective dynamics and an amplifier dynamics along the shear layer. The most energetic dynamics originate from shear instabilities which are predominant for frequencies lower than $\omega \approx 2.6$. What is of utmost importance is to note that the singular value decomposition of the resolvent leads to a decomposition in the frequency domain which optimally orders the set of forcing (inputs) and associated responses (outputs). Notably, this decomposition highlights the most energetic part of the map linking all possible inputs to all possible outputs in the frequency interval of interest. From a physical point of view, the present analysis highlights the linear physical mechanisms at play in a backward-facing step flow: the Orr and Kelvin–Helmholtz instabilities amplify upstream perturbations for $\omega < 2.6$, while perturbations in the free stream are simply advected downstream.

4. Dynamics of the flow subjected to a stochastic forcing

In realistic configurations, external disturbances are not likely to be harmonic but rather characterized by a broadband frequency spectrum. Assuming that the flow is excited by a random noise, only characterized by its statistical properties, an important point is to identify which mechanisms naturally emerge. We partially answer this question by computing the flow structures which optimally account for the variance of the resulting random flow field (the EOFs) and by computing the forcing structures that optimally trigger this flow field (the SOs). These flow structures are expressed

as a function of the optimal forcing and responses introduced in the previous section: hence, we manage to link stochastic features (the EOFs and SOs) to the various instability mechanisms at play in the flow (the optimal forcing/responses).

4.1. *Empirical orthogonal functions*

Truncating a flow dynamics to its most energetic patterns is common in studies of turbulence (see Berkooz *et al.* 1993). The most energetic patterns are usually referred to as POD modes or also EOFs.

The idea consists of artificially forcing system (2.2) by a stochastic process and extracting dynamical information from the flow response. This response can then be decomposed and ranked by the leading energetic coherent processes. We consider the dynamics of the stochastically forced system given by

$$\dot{\boldsymbol{x}} = \boldsymbol{A}\,\boldsymbol{x} + \boldsymbol{F}\xi(t) \tag{4.1}$$

where $\boldsymbol{F}$ is a matrix of size $n \times n$ governing the structure of the forcing. Furthermore, the vector $\xi(t)$ of size $n \times 1$ is chosen as a space–time Gaussian white noise process with zero mean, such that $[\xi_i(t)] = 0$ and $[\xi_i(t)\xi_j(t')] = \delta_{ij}\delta(t - t')$ where $[\,]$ denotes the ensemble average and δ_{ij} the Kronecker symbol. The ith component $\xi_i(t)$ of the noise is defined so as to force the ith column of the matrix $\boldsymbol{F}$. We assume that $\boldsymbol{F}$ is a unitary matrix ($\boldsymbol{F}^\dagger\boldsymbol{F} = \boldsymbol{I}$) so that its columns are orthogonal; the forcing is defined as the sum of an orthonormal set of uncorrelated processes. As mentioned by Fontane *et al.* (2008), a spatial covariance matrix representing a true experimental noise environment may also be used in order to represent more specific perturbation fields. In our case, we assume that no information on the noise is available and keep the above-mentioned formulation so as to mimic the most generic unknown disturbances in an unbiased manner.

In the presence of the permanent random excitation, the dynamics of the random flow state $\boldsymbol{x}(t)$ is governed by (4.1). Since the flow is globally stable ($\boldsymbol{A}$ is stable), the solution of this problem tends to a statistically steady state for sufficiently large times. Furthermore, as shown by Farrell & Ioannou (1993*a*, 1996), this statistically steady flow state can be characterized by its covariance matrix $\boldsymbol{P} = [\boldsymbol{x}(t)\boldsymbol{x}\,(t)^\dagger]$ which is independent of $\boldsymbol{F}$ and reduces to

$$\boldsymbol{P} = \int_0^{+\infty} \mathrm{e}^{\boldsymbol{A}t}\mathrm{e}^{\boldsymbol{A}^\dagger t}\,\mathrm{d}t. \tag{4.2}$$

This matrix is Hermitian so that its eigenvectors form an orthogonal basis. These eigenvectors are the so-called EOFs. By construction, the leading EOFs correspond to the flow structures which optimally account for the variance of the statistically steady state, see Farrell & Ioannou (1993*a*). Indeed, assuming that the ith EOF φ_i is associated with the eigenvalue β_i and that the random state $\boldsymbol{x}(t)$ is decomposed in the sum

$$\boldsymbol{x}(t) = \sum_{i=1}^{n} \alpha_i(t)\varphi_i \tag{4.3}$$

then it can be shown that the expansion coefficients $\alpha_i(t)$ are scalar uncorrelated random variables: $[\alpha_i(t)\alpha_j(t')] = \delta_{ij}\delta(t - t')\beta_i$. Notably, the variance of the coefficients α_i are equal to the eigenvalues of φ_i. Therefore, the trace of the covariance matrix reduces to the total variance maintained in the statistically steady state. Since the space–time dynamics of the EOFs are uncorrelated from each other, they are

commonly interpreted as coherent processes of the flow field. In other words, the random flow field $\boldsymbol{x}(t)$ with known covariance is decomposed in (4.3) as a family of coherent processes evolving in parallel. Energy is furthermore mostly carried by the leading eigenvectors which make them a preferred basis of functions for the truncation of dynamical systems.

4.1.1. *Computation*

For a problem of small size, the covariance matrix $\boldsymbol{P}$ can be directly computed from a Lyapunov equation, see Farrell & Ioannou (1993*a*, 2001). However, in our case, solving such an equation is not tractable. An alternative approach has to be employed to compute the leading EOFs without requiring to compute or even store the matrix $\boldsymbol{P}$. The technique introduced here enables to overcome this difficulty and is based on the frequency domain decomposition of the dynamics presented in § 3.

Using Parseval's theorem, we may rewrite $\boldsymbol{P}$ in the frequency space and discretize the integral:

$$\boldsymbol{P} = \frac{1}{2\pi}\int_{-\infty}^{\infty} \boldsymbol{R}(\omega)\boldsymbol{R}^{\dagger}(\omega)\,\mathrm{d}\omega = \frac{1}{2\pi}\sum_{i\in\mathbb{Z}} \boldsymbol{R}(\omega_i)\boldsymbol{R}^{\dagger}(\omega_i)\delta_i \tag{4.4}$$

where $\{\omega_i,\ \ i\in\mathbb{Z}\}$ is a given set of discrete frequencies and δ_i denotes appropriate quadrature coefficients. $\boldsymbol{P}$ reduces to the sum of the matrices $\boldsymbol{R}(\omega_i)\boldsymbol{R}^{\dagger}(\omega_i)$, which cannot be computed or stored. To alleviate this limitation, an approximation is performed. These matrices are replaced by their truncated eigenvalue decomposition:

$$\boldsymbol{R}(\omega_i)\boldsymbol{R}^{\dagger}(\omega_i) \approx \boldsymbol{X}(\omega_i)\Lambda\,(\omega_i)^2\,\boldsymbol{X}^{\dagger}(\omega_i) \tag{4.5}$$

where $\boldsymbol{X}(\omega_i)$ and $\Lambda\,(\omega_i)^2$ are the matrices of leading eigenvectors and eigenvalues, respectively. For an approximation of rank k, $\boldsymbol{X}(\omega_i)$ is a $n\times k$ complex matrix satisfying $\boldsymbol{X}^{\dagger}(\omega_i)\boldsymbol{X}(\omega_i)=\boldsymbol{I}_k$ whereas $\Lambda(\omega_i)$ is a $k\times k$ real diagonal matrix. The rank k is thus a fundamental parameter to assess the efficiency of this approximation. Note that the columns of $\boldsymbol{X}(\omega)$ reduce to the left singular vectors of $\boldsymbol{R}(\omega)$ and also to the optimal responses previously denoted by $\hat{\boldsymbol{x}}_i(\omega)$ (see (3.2)). Furthermore, the diagonal elements $\lambda_i(\omega)$ of matrix $\Lambda(\omega)$ are the leading singular values of $\boldsymbol{R}(\omega)$ introduced in (3.1). The approximation given in (4.5) is more accurate when the optimal gains λ_i^2 fall off quickly. This property may be assessed by looking at figure 2. Then by using decomposition (4.5), we obtain a low-rank approximation of the covariance matrix $\boldsymbol{P}$ such that

$$\boldsymbol{P} = \boldsymbol{X}\boldsymbol{X}^{\dagger} \tag{4.6}$$

where the real matrix $\boldsymbol{X}$ is obtained by stacking the real and imaginary parts of the flow states $\boldsymbol{X}\Lambda$ on a finite interval of positive frequencies ω_i with appropriate quadrature coefficients. As a result, for a set of n_ω positive frequencies, $\boldsymbol{X}$ is of size $n\times 2kn_\omega$. It is then possible to recover the leading eigenvalues/vectors of $\boldsymbol{P}$ by using the classical snapshot technique introduced by Berkooz *et al.* (1993). First, we perform the eigenvalue decomposition $\boldsymbol{X}^{\dagger}\boldsymbol{X} = \boldsymbol{H}\boldsymbol{B}\boldsymbol{H}^{*}$, where the diagonal matrix $\boldsymbol{B}$ contains the leading eigenvalues β_i associated with the EOFs, namely the leading eigenvalues of $\boldsymbol{P}$. The leading EOFs φ_i are computed by

$$\varphi_i = \beta_i^{-1/2}\boldsymbol{X}\boldsymbol{H}_i \tag{4.7}$$

where $\boldsymbol{H}_i$ denotes the ith column of the matrix $\boldsymbol{H}$. Note that the EOFs are orthogonal by construction, namely $\varphi_i^{\dagger}\varphi_j = \delta_{ij}$. Importantly, (4.7) expresses the EOFs as a linear

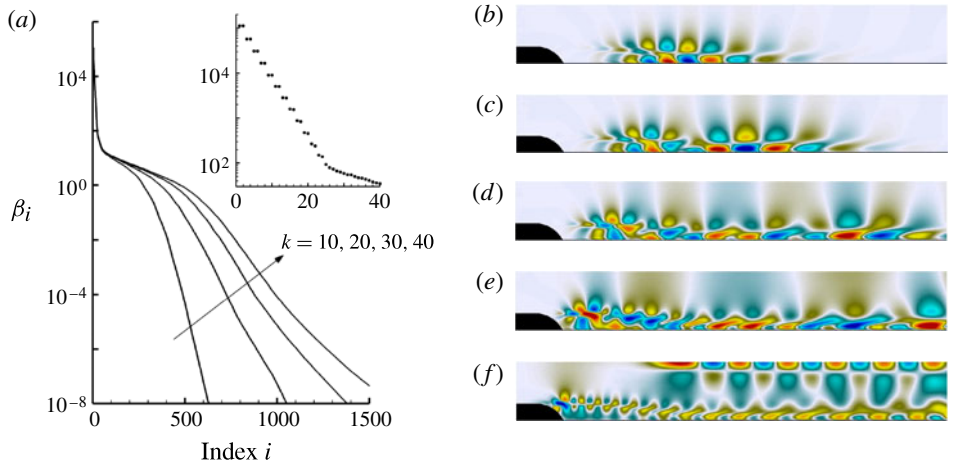

FIGURE 7. (*a*) First 1500 eigenvalues β_i. (*b–f*) Longitudinal velocity of the 1st, 3rd, 9th, 18th and 40th empirical orthogonal functions.

combination of the optimal harmonic responses over a given frequency range. The procedure introduced here is meant to optimally approximate the leading EOFs from the subset of the k leading optimal harmonic responses.

4.1.2. *Results*

The computation of the EOFs is based on the optimal responses described in § 3. To discretize the frequency-domain integral defined in (4.4), an equidistant spacing between 129 frequencies in $\omega \in [0; 4]$ has been adopted and quadrature coefficients corresponding to the fourth-order Simpson method have been used. Note that the rank k of truncation has to be carefully taken into consideration to assess the accuracy of the approximation.

We have represented in figure 7(*a*) the first 1500 eigenvalues β_i for various values of the approximation rank $k = 10, 20, 30$ and 40. The leading eigenvalues are observed to be converged when increasing the value of k and this also holds for the associated eigenvectors (not shown here). In addition, figure 7(*a*) provides a zoom on the first 40 eigenvalues, which are converged in terms of the rank k. The first eigenvalues come in pair which indicates that the most significant EOFs account for travelling structures. Furthermore, the leading eigenvalues fall off quite rapidly, indicating that the flow response to stochastic forcing is only driven by a low number of coherent processes. We have represented in figure 7(*b–f*) the longitudinal velocity of the 1st, 3rd, 9th, 18th and 40th EOFs, respectively. They appear as wave packets that spatially extend downstream, where the response energy to forcing is largest. In contrast to the optimal responses discussed in § 3, the EOFs are not associated with particular frequencies. Rather, they represent the most energetic patterns emerging from a white noise forcing which excites all of the frequencies and spatial wavelengths in an equal balance. Interestingly, the first EOF is characterized by the same streamwise wavelength as that of the optimal flow response at $\omega = 0.75$. This observation confirms that the forcing of all space–time scales results in a preferred frequency of $\omega = 0.75$ in the flow response, see figure 2. As for higher EOFs, their spatial support is observed to extend farther downstream. Furthermore, they display more complex structures characterized by more

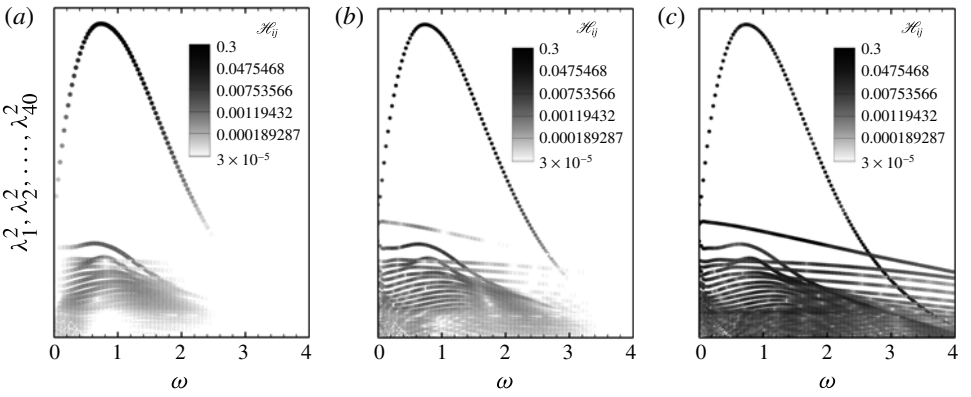

FIGURE 8. First 40 optimal energy gains λ_i^2 versus frequency ω colour-coded by the factor $\mathscr{H}_{ij}$. (*a–c*) Case of the 1st, 9th and 40th EOF. Note that the values of $\mathscr{H}_{ij}$ are all displayed with the same logarithmic scale.

than one particular wavelength. In particular, smaller structures are observed near separation while larger structures are mainly localized downstream, see figure 7(*e,f*).

As mentioned previously, the EOFs represent uncorrelated energy-ranked flow states so that the jth EOF contributes to $\beta_j / \sum_{i=1}^{n} \beta_i \times 100\,\%$ of the total sustained variance. As an indicative illustration, the first 4 EOFs contain 71 % of the total variance while the first 10 EOFs contain 94 % of it (independently of the rank k).

Identifying the leading EOFs is only the first step when investigating the dynamics of the random flow. Indeed, the EOFs may be further linked to physical mechanisms and/or frequency intervals. We already mentioned that the EOFs are obtained from linear combinations of optimal responses, see (4.7). In fact, for a given EOF, it is possible to identify the weight, or contribution, of each response thanks to the coefficients of matrix $\boldsymbol{H}$. Let us consider the jth EOF. It is expressed as a linear combination of the real and imaginary parts of k optimal responses for n_ω frequencies in $\omega \in [0; 4]$:

$$\varphi_j = \frac{1}{\sqrt{\beta_j}} \sum_{i=1}^{2kn_\omega} \boldsymbol{X}_i \boldsymbol{H}_{ij} \tag{4.8}$$

where $\boldsymbol{X}_i$ denotes the ith column of matrix $\boldsymbol{X}$. As a result, the weight of the optimal responses may be evaluated by the factors $\boldsymbol{H}_{ij}$. Assuming the real and imaginary parts of the ith optimal response are stacked in the $(2i-1)$th and $(2i)$th columns of $\boldsymbol{X}$, then the quantity $\mathscr{H}_{ij} = \sqrt{\boldsymbol{H}_{(2i-1)j}^2 + \boldsymbol{H}_{(2i)j}^2}$ accurately assesses the contribution of the ith optimal response to the jth EOF.

This criterion has been computed for various EOFs for $k = 40$. Results are shown in figure 8, which depicts the leading 40 energy gains λ_i^2 versus frequency ω, coloured by the factor $\mathscr{H}_{ij}$ of its associated optimal response. In figure 8(*a–c*) the case of the 1st, 9th and 40th EOF are considered respectively. As for the first EOF, a large and predominant contribution of the responses in branch $A1$, within the frequency range $\omega \in [0.5; 1.3]$ is observed. In particular, the highest contribution is obtained on this branch for $\omega \approx 0.75$. This result explains why the first EOF is so similar to the overall optimal response depicted in figure 3(*d*). Furthermore, we clearly notice a minor, yet noticeable, contribution from the suboptimal responses associated with shear branches.

On the other hand, optimal responses associated with convective branches have no contribution. This result means that the first EOF, which predominantly accounts for the random flow dynamics, is mainly driven by Kelvin–Helmholtz shear instability mechanisms in the frequency range $\omega \in [0.5; 1.3]$.

Now, let us consider the ninth EOF, see figure 8(*b*). This mode still displays a large contribution from shear mechanisms, but also a noticeable contribution from convective branches associated with free stream dynamics. Furthermore, these contributions are distributed among wider frequency ranges. The predominant contribution still comes from branch $A1$, in the frequency range $\omega \in [0.2; 1.6]$. Finally, the case of the 40th EOF is depicted in figure 8(*c*). We observe that the contributions $\mathscr{H}_{ij}$ are even more distributed among the spectrum of optimal responses. In particular, shear branches display similar contributions to those of convective branches. Furthermore, the highest contribution is obtained on the convective branch $B1$ for $\omega \approx 1.66$. In a more general manner, we observe more distributed contributions for higher EOFs: more branches are involved in the dynamics and on wider frequency ranges.

The above-described analysis illustrates one of the major interest of our formulation i.e. the possibility to link the most energetic process of a randomly forced flow to: (i) specific frequency intervals; and (ii) specific instability mechanisms. In other words, the procedure allows to quantify, rank and organize the leading instability mechanisms at play in randomly forced stable flows. As a result, such an analysis may provide an additional tool for the post-processing of experimental data; by linking the coherent structures of a random flow to the canonical physical mechanisms at play.

4.2. *Stochastic optimals*

Owing to the non-normality of the linear operator for this base flow, it is known that the optimal responses of the flow are structurally distinct from the corresponding optimal excitations, see Farrell & Ioannou (2001). In particular, the set of forcing distributions yielding a maximum contribution to the variance of the statistically steady state differs from the EOFs and are called SOs. Investigating the SOs is important as it provides information on which structures optimally excite the instabilities of the flow.

Considering system (4.1) with orthogonal forcing structures $\boldsymbol{F}$, the maintained variance can be expressed, see Farrell & Ioannou (1993*a*), by $[x^\dagger x] = \mathrm{trace}(\boldsymbol{F}^\dagger \boldsymbol{Q} \boldsymbol{F}) = \mathrm{trace}(\boldsymbol{Q})$ where the matrix $\boldsymbol{Q}$ is defined by

$$\boldsymbol{Q} = \int_0^{+\infty} \mathrm{e}^{\boldsymbol{A}^\dagger t} \mathrm{e}^{\boldsymbol{A} t} \, \mathrm{d}t. \tag{4.9}$$

This matrix is also Hermitian so that its eigenvectors are orthogonal. They rank the forcing structures, i.e. the columns of $\boldsymbol{F}$, by their contribution to exciting the maintained variance. Let ϕ_i be the ith eigenvector of $\boldsymbol{Q}$ with its eigenvalue γ_i and κ_i be a set of scalars, then a forcing given by $\sum_{i=1}^{n} \kappa_i \phi_i \xi_i(t)$ with $[\xi_i(t)\xi_j(t')] = \delta_{ij}\delta(t - t')$ will lead for large times to a statistically steady flow state of variance equal to $\sum_{i=1}^{n} \kappa_i^2 \gamma_i$

In other words, the variance sustained by the ith eigenvector at statistical equilibrium is proportional to the eigenvalue γ_i and the total variance is related to the trace of $\boldsymbol{Q}$. Consequently, any random forcing can be decomposed as a family of uncorrelated and orthogonal coherent processes ranked by their contribution to the evolved flow state sustained variance. In other words, energy is mostly triggered by the excitation of the dominant stochastic optimals.

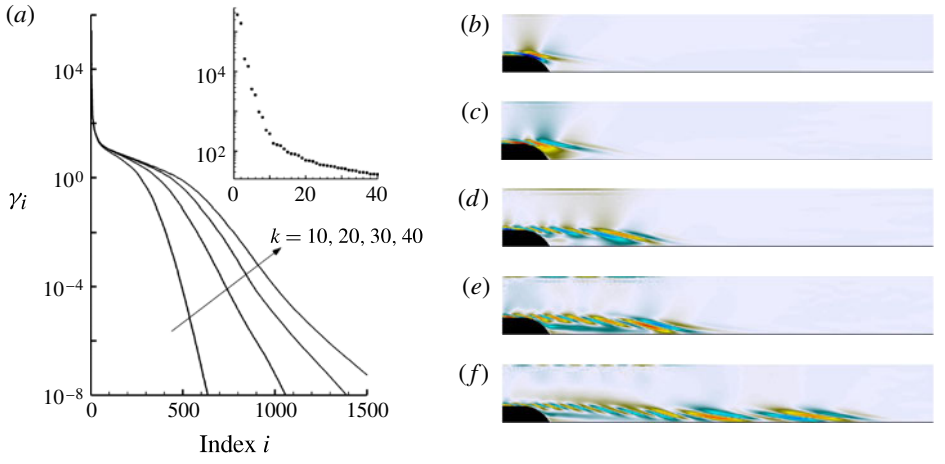

FIGURE 9. (*a*) First 1500 eigenvalues γ_i. (*b–f*) Depict the longitudinal velocity of the 1st, 3rd, 9th, 16th and 30th SOs.

4.2.1. *Computation*

The computation of the leading eigenvectors of $\boldsymbol{Q}$ involves the same numerical technique as that of $\boldsymbol{P}$. $\boldsymbol{Q}$ is written in the frequency domain, the integral is discretized thanks to quadrature coefficients, and the operators $\boldsymbol{R}^\dagger(\omega_i)\boldsymbol{R}(\omega_i)$ are approximated by $\boldsymbol{Y}(\omega_i)\Lambda(\omega_i)^2\boldsymbol{Y}^\dagger(\omega_i)$ where $\boldsymbol{Y}(\omega_i)$ comprises the optimal harmonic forcing previously denoted by $\hat{\boldsymbol{f}}_i(\omega)$ (see (3.1)) and $\Lambda(\omega_i)^2$ the optimal energy gains at the frequency ω. This then leads to a low-rank approximation of the matrix $\boldsymbol{Q}$:

$$\boldsymbol{Q} = \boldsymbol{Y}\boldsymbol{Y}^\dagger \tag{4.10}$$

where the real matrix $\boldsymbol{Y}$ is built by stacking with the above-mentioned quadrature coefficients the real and imaginary parts of the states $\boldsymbol{Y}(\omega_i)\Lambda(\omega_i)$ on a finite interval of positive frequencies ω_i. The leading eigenvalues of $\boldsymbol{Q}$ are denoted γ_i and the associated stochastic optimals ϕ_i.

4.2.2. *Results*

We have depicted in figure 9(*a*) the first 1500 eigenvalues γ_i for different values of the approximation rank k. The cases $k = 10, 20, 30$ and 40 have been investigated. Analogously, the leading eigenvalues are observed to be converged when increasing the parameter k. Furthermore, the leading eigenvalues also come in pairs and fall off rapidly. Consequently: (i) the first SOs are travelling patterns that are 90° out of phase; and (ii) only a low number of forcing structures have a significant contribution to the evolved sustained variance. Figure 9(*b–f*) represents the 1st, 3rd, 9th, 16th and 30th SOs, respectively. As one could expect, the leading SOs reduce to upstream located structures. This result is consistent and further illustrates the spatial separation between optimal forcing and optimal responses in open flows, see Brandt *et al.* (2011). Notably, they display flow structures that are inclined against the shear so as to take advantage of the Orr mechanism to optimally extract energy from the base flow.

Since SOs yield a basis of uncorrelated forcing ranked by their energy contribution, it is interesting to assess the part of the total energy resulting from the leading ones. For all of the values of k investigated, the first 4 modes lead to 97 % of the total evolved variance while the first 10 modes yield ∼99 % of it.

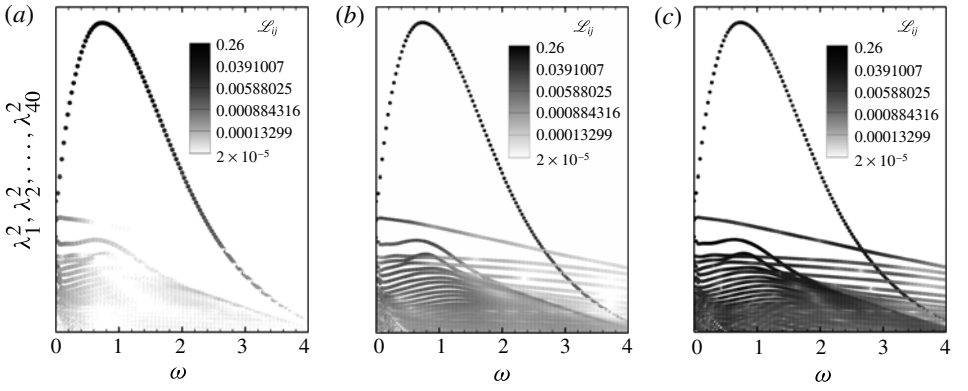

FIGURE 10. First 40 optimal energy gains λ_i^2 versus frequency ω colour-coded by the factor $\mathscr{L}_{ij}$. (*a–c*) Case of the 1st, 9th and 30th SOs. Note that the values of $\mathscr{L}_{ij}$ are all displayed with the same logarithmic scale.

Similarly to the analysis of EOFs, SOs may be further linked with instability mechanisms by assessing the contribution of each optimal forcing by computing the quantity $\boldsymbol{L}_{ij}$, similar to $\boldsymbol{H}_{ij}$.

This quantity has been computed for the leading SOs with $k = 40$ and the results are shown in figure 10. Analogously to figure 8, the leading 40 energy gains versus frequency, colour-coded by the factor $\mathscr{L}_{ij}$ are represented. The case of the 1st, 9th and 30th SOs are represented in figure 10(*a–c*). The first SO displays a large and predominant contribution from the forcing fields in branch $A1$, in the frequency range $\omega \in [0.3; 1.4]$. In addition, the highest contribution stems from the forcing at $\omega \approx 0.75$ on this branch. All other branches only add a small contribution to the first SO, within the lowest frequencies. Thus, the first SO, i.e. the structure the most sensitive to stochastic forcing is found to predominantly exploit the Kelvin–Helmholtz instability mechanism in the frequency interval $\omega \in [0.3; 1.4]$. In other words, the maximum variability of the flow may be obtained from the optimal excitation of this instability in this frequency range.

Regarding higher SOs, their contributions are much more distributed among the other branches and frequencies. For instance, let us examine the case of the ninth SO depicted in figure 10(*b*). Its predominant contributions still stem from branch $A1$ but in a much wider frequency range $\omega \in [0.1; 2.3]$. In addition, all other branches including the convective branches are observed to add a low but noticeable contribution on all frequencies. As for the 30th SO, we have represented the results in figure 10(*c*). Similarly, its contributions are observed to be widely distributed among all frequencies. However, its highest contributions are found to be associated with shear branches, and more particularly to branch $A2$.

Finally, we have shown how the procedure allows us to link the leading SOs to specific instabilities and/or frequency intervals. In other words, we have shown how to rank and organize the forcing fields that are most sensitive to stochastic forcing as a function of the canonical instability mechanisms at play. Hence, such an analysis may provide an additional tool to investigate the receptivity of stable open flows; it would be complementary to optimal perturbation and optimal forcing/response analyses.

4.3. *Assessment and discussion*

We have shown how to relate the leading EOFs/SOs to the optimal harmonic forcing and responses of the flow. In fact, the EOFs/SOs may be seen as barycentres of the set of optimal forcing and responses and the weight of each optimal state yields information on its contribution to the considered EOF/SO. According to the study of § 3, the flow is mainly receptive to shear instability mechanisms in the frequency range $\omega \in [0; 2.6]$. Now, considering a random forcing which favours neither any particular region of the flow nor any frequency, it is not surprising to obtain leading EOFs/SOs which describe the same dynamics. We naturally do not expect to observe this correspondence when considering more specific noise distributions. The present procedure may be even more informative and useful in the case of more complex flow configurations having more than one predominant instability mechanism. Notably, the application of our procedure may be particularly interesting for turbulent flows. Indeed, the present methodology and computations may be easily extended to the Navier–Stokes equations augmented by a turbulence model. Such models are based on the assumption that the dynamics of the small and large scales are decoupled. The small scales (high frequencies) are assumed to be accounted for by the turbulence model whereas the dynamics of the large scales (low frequencies) are governed by the time integration of the equations, see the previous works by Crouch, Garbaruk & Magidov (2007) and Cossu, Pujals & Depardon (2009). As a result, the linear dynamics of perturbations about the mean flow may govern the large-scale structures within the turbulent flow. Thereby, the leading EOFs obtained from such turbulent models would account for the large-scale coherent structures that would naturally emerge from the turbulent flow. Similarly, the leading SOs would represent the large-scale spatial patterns that are most sensitive to a low-frequency stochastic excitation of the flow such as upstream noise or residual turbulence.

5. Model reduction

We now turn our attention to the model reduction of the flow dynamics. We seek a reduced-order state-space model which captures the dynamics from all possible inputs to all possible outputs. The model is obtained by a Galerkin projection of the governing equation (2.2) onto the subspace spanned by a basis of modes. We will consider in the following bases made out with EOFs, SOs and balanced modes. In our case, all of the degrees of freedom of system (2.2) are inputs and outputs. In such a case, it can be shown (Farrell & Ioannou 2001) that the controllability and observability Gramians correspond to the operators $\boldsymbol{P}$ and $\boldsymbol{Q}$, respectively. Therefore, the EOFs and SOs coincide with the most controllable and observable modes. The balanced modes are defined as the leading eigenvectors of the product $\boldsymbol{PQ}$. To compute these structures, we consider the low-rank approximations of the Gramians based on the optimal forcing/response given in (4.6) and (4.10). Following the algorithm introduced by Laub *et al.* (1987), we perform the singular value decomposition of the cross-product $\boldsymbol{Y}^{\dagger}\boldsymbol{X}$. This matrix is dense and of size $2kn_\omega \times 2kn_\omega$, where n_ω is the number of discretized frequencies and k the number of optimal forcing/response kept in the approximation of the resolvent at each frequency. The direct and adjoint balanced modes are then straightforwardly obtained from this computation. It should be emphasized that the present algorithm is similar to the method of snapshots introduced by Rowley (2005), except that the low-rank approximations of the Gramians are not obtained by time snapshots but by singular value decompositions of the resolvent operator.

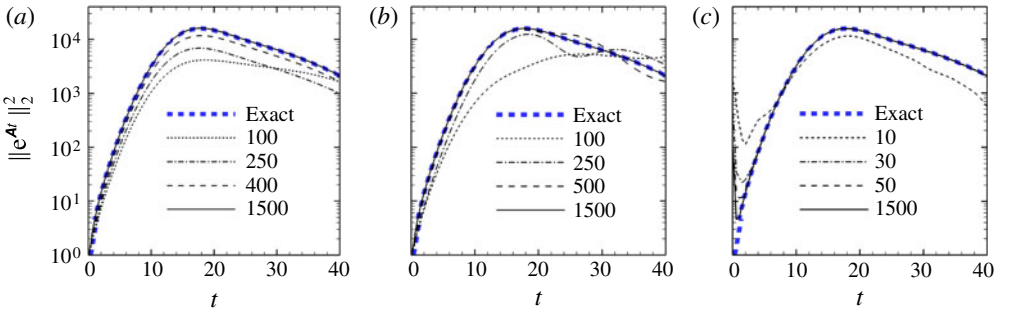

FIGURE 11. Optimal perturbation gain $\|e^{\boldsymbol{A}t}\|_2^2$ at time t for ROMs based on: (*a*) EOFs; (*b*) SOs; and (*c*) balanced modes.

In the following, we consider a primal and a dual basis $\boldsymbol{T}$ and $\boldsymbol{S}$, made out of the EOFs, SOs or balanced modes. $\boldsymbol{S}$ and $\boldsymbol{T}$ are rectangular matrices of dimension (n, r), where r is the size of the reduced basis. The bases $\boldsymbol{T}$ and $\boldsymbol{S}$ satisfy the bi-orthogonality condition $\boldsymbol{S}^\dagger\boldsymbol{T} = \boldsymbol{I}$. The dynamics in the reduced basis is given by the matrix $\boldsymbol{A}_r = \boldsymbol{S}^\dagger\boldsymbol{A}\boldsymbol{T}$ of size (r, r).

5.1. *Performance in the time domain*

First, we examine the ability of the ROMs to recover the original time propagator. To this end, we proceed as in the previous works by Ehrenstein & Gallaire (2005), Åkervik *et al.* (2008) and Alizard *et al.* (2009) by evaluating the optimal energy gain in time over all possible initial conditions and the associated optimal perturbations. The maximum energy gain over all possible initial conditions at time t is obtained by considering the maximum eigenvalue of $e^{\boldsymbol{A}^\dagger t}e^{\boldsymbol{A}t}$, the associated eigenvector being the optimal initial condition. This quantity corresponds to the square of the 2-norm of the matrix $e^{\boldsymbol{A}t}$ ($\|e^{\boldsymbol{A}t}\|_2^2$), and may be computed for the full system by using the iterative algorithm and numerical methods used by Marquet *et al.* (2008).

As for the ROMs, we proceed by computing the optimal energy gain of the high-dimensional low-rank time propagator $\boldsymbol{T}e^{\boldsymbol{A}_r t}\boldsymbol{S}^\dagger$. For this, we look for the optimal initial condition $\boldsymbol{x}_0$ in the dual basis, $\boldsymbol{x}_0 = \boldsymbol{S}\tilde{\boldsymbol{x}}_0$. We are led to the following eigenproblem:

$$\boldsymbol{N}e^{\boldsymbol{A}_r^\dagger t}\boldsymbol{M}e^{\boldsymbol{A}_r t}\boldsymbol{N}\tilde{\boldsymbol{x}}_0 = \mu^2\boldsymbol{N}\tilde{\boldsymbol{x}}_0 \tag{5.1}$$

which may easily be solved with standard methods since it only involves low-dimensional quantities, $\boldsymbol{A}_r$, $\boldsymbol{M} = \boldsymbol{T}^\dagger\boldsymbol{T}$ and $\boldsymbol{N} = \boldsymbol{S}^\dagger\boldsymbol{S}$. The optimal energy gain $\|\boldsymbol{T}e^{\boldsymbol{A}_r t}\boldsymbol{S}^\dagger\|_2^2$ corresponds to the largest eigenvalue μ^2 of (5.1). It is represented in figure 11 for models based on: (*a*) EOFs; (*b*) SOs; and (*c*) balanced modes. These results have been obtained with $n_\omega = 129$ and $k = 40$. In all cases, we observe a convergence to the original optimal curve displayed by a bold dashed line; the overall optimal energy gain exceeds 10^4 and is reached for an optimal time $t = 18$. It should be pointed out that the large gain values obtained near $t = 0$ with the balanced modes are not physical: all ROMs are inaccurate at short times if the initial condition does not belong to the subspace spanned by the primal basis. This is precisely the case for the balanced models since the optimal initial condition is looked for in the dual basis and the dual basis is different from the primal one. For larger time values, balanced models are much more effective as they recover the main energy peak with

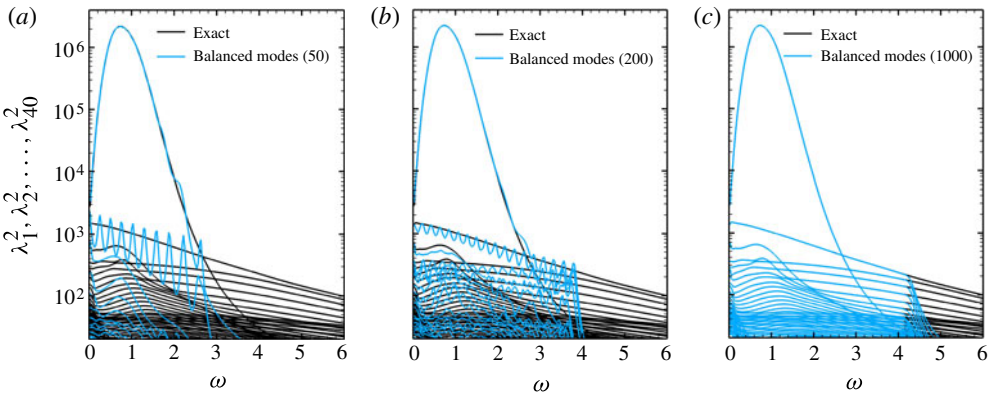

FIGURE 12. First 40 optimal energy gains versus frequency ω computed for the full system (λ_i^2) and ROMs (μ_i^2). Parts (a–c) show models based on 50, 200 and 1000 balanced modes, respectively.

much fewer modes ($\sim$30 instead of $\sim$1000). This result is consistent since we expect balanced modes to quasi-optimally capture the flow dynamics.

5.2. *Performance in the frequency domain*

We now assess the ability of the ROMs to recover the optimal and suboptimal energy gains of the resolvent operator. The optimal energy gains of the ROMs are defined as the square of the largest singular values of the low-rank resolvent $\boldsymbol{R}_{lr} = \boldsymbol{T}\boldsymbol{R}_r\boldsymbol{S}^\dagger$ where $\boldsymbol{R}_r = (\mathrm{i}\omega\boldsymbol{I}_r - \boldsymbol{A}_r)^{-1}$. Similarly to the case of optimal initial perturbations, the forcing is looked for in the subspace spanned by the dual basis, $\hat{\boldsymbol{f}} = \boldsymbol{S}\tilde{\boldsymbol{f}}$. We therefore solve for the largest eigenvalues μ_i^2 of

$$\boldsymbol{N}\boldsymbol{R}_r^\dagger\boldsymbol{M}\boldsymbol{R}_r\boldsymbol{N}\tilde{\boldsymbol{f}}_i = \mu_i^2\boldsymbol{N}\tilde{\boldsymbol{f}}_i. \tag{5.2}$$

In figure 12, we compare, for $k = 40$, the first 40 optimal gains of the reduced models ($\mu_1^2, \ldots, \mu_{40}^2$) to those of the large-scale problem ($\lambda_1^2, \ldots, \lambda_{40}^2$) as a function of frequency. Figure 12(a–c) is respectively concerned with ROMs based on 50, 200 and 1000 balanced modes. The optimal energy gains computed from the ROMs are observed to converge to the exact ones when increasing the size of the models. Furthermore, this result holds for the associated singular vectors, i.e. the optimal forcing/responses (not shown here). Not only the 'shear layer' branches are captured by the models but also the 'convective' ones. All of the leading singular values are well reproduced until the cut-off frequency $\omega \approx 4$. This limitation is consistent since the projection bases have been computed from a linear combination of harmonic optimals within $\omega \in [0; 4]$. To extend this range, one has to consider additional optimal forcing/response when computing the projection bases. Results (not shown here) pertaining to EOFs' and SOs' bases show trends which are similar to those presented for the time propagator: they also manage to reproduce the optimal gains but much more modes are required.

5.3. *Error quantification*

The efficiency of the ROMs to recover the original dynamics may be quantified by computing a global error, the ∞-norm of the difference between the resolvent

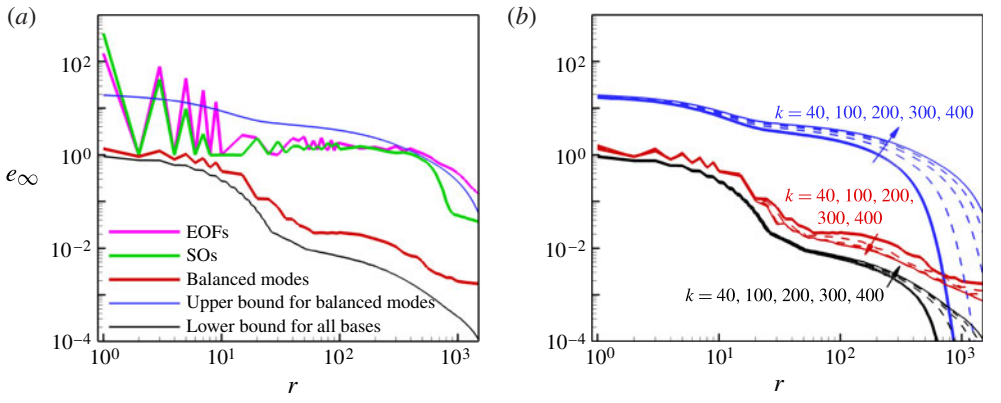

FIGURE 13. Relative ∞-norm error as a function of the size r of the ROMs. (*a*) Error for models based on EOFs, SOs and balanced modes with $k = 40$, as well as the error bounds for $k = 400$. (*b*) Assessment of the convergence of the error of the balanced models and of the upper and lower error bounds with k.

operators. Denoting the low-rank resolvent $\boldsymbol{R}_{lr} = \boldsymbol{T}\boldsymbol{R}_r\boldsymbol{S}^\dagger$, the relative error is defined as

$$e_\infty(r) = \frac{|||\boldsymbol{R}_{lr} - \boldsymbol{R}|||_\infty}{|||\boldsymbol{R}|||_\infty} \tag{5.3}$$

with $|||\boldsymbol{R}|||_\infty = \max_\omega \|\boldsymbol{R}(\omega)\|_2$.

The computation of the quantity $|||\boldsymbol{R}_{lr} - \boldsymbol{R}|||_\infty$ involves the evaluation of $\|\boldsymbol{R}_{lr}(\omega) - \boldsymbol{R}(\omega)\|_2$ at given frequencies ω. For this, we look for the eigenvalue of the matrix $(\boldsymbol{R}_{lr}^\dagger(\omega) - \boldsymbol{R}^\dagger(\omega))(\boldsymbol{R}_{lr}(\omega) - \boldsymbol{R}(\omega))$. Again a Lanczos method is used associated with a direct LU sparse solver for the inverses involved in $\boldsymbol{R}(\omega)$ and $\boldsymbol{R}^\dagger(\omega)$ and a standard LAPACK routine for the inverses involved in $\boldsymbol{R}_{lr}(\omega)$ and $\boldsymbol{R}_{lr}^\dagger(\omega)$. We have represented in figure 13(*a*) the relative error e_∞ as a function of the size r of the models, in the case $k = 40$. We observe a clear and rather monotonous decrease of the error in the case of balanced modes, until a relative error of $\sim$0.15 % is reached at $r = 1500$. We also clearly see in figure 13(*a*) that the relative error obtained with balanced models lies between the standard (Rowley 2005) upper and lower theoretical bounds (obtained with $k = 400$, see below). In the case of EOFs and SOs, the models display worse results. The relative errors oscillate until $r \approx 400$; then they start to decrease to reach 15 and 3.5 %, respectively, at $r = 1500$.

As one could expect, the balanced modes provide the best results. This is not surprising since balanced truncation is meant to minimize this error. We now check that our results are converged in terms of the number k of singular values that were kept at each frequency for the approximation of the Gramians. Note that for k greater than 40, we use SCALAPACK to compute the singular values of $\boldsymbol{Y}^\dagger\boldsymbol{X}$. For $k = 400$ the size of the matrices reaches $10^5 \times 10^5$: we used 440 processors, the singular values and vectors being obtained in less than 15 h, 2 GB of memory residing on average on each processor. We have represented in figure 13(*b*) the relative error e_∞ and the standard error bounds as a function of r. Several curves are displayed for different values of k: $k = 40, 100, 200, 300, 400$. In this study, the number of frequencies n_ω has been kept constant and equal to 129. For k ranging from 40 to 400, we observe that the lower and upper error bounds slightly increase for large values of r while the relative error of the balanced models slightly decreases. Further, the relative error curve gets closer

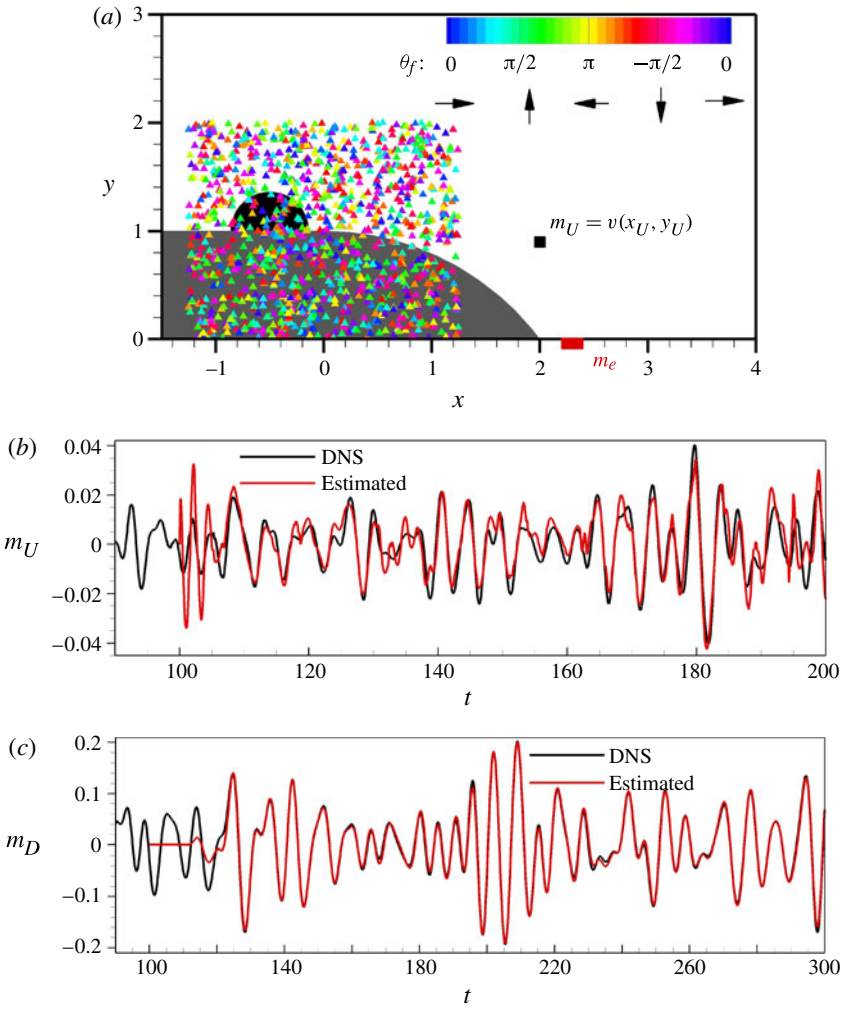

FIGURE 14. Example of the data assimilation problem. (*a*) Sketch of the forcing environment (small triangles). The black half-circle depicts the estimated noise that is used in the design of the Kalman filter. The estimation sensor m_e is shown with a rectangle (shown in red in the online version), while the black square represents the location of the upstream testing sensor m_U. (*b*) Comparison for sensor m_U between the true signal and the reconstructed one by the estimator. (*c*) Same but for sensor m_D, which extracts the cross-stream velocity component at the downstream location ($x_D = 12$, $y_D = 0.15$).

to the lower bound, which shows that the relative error of the balanced models tends to the lowest bound achievable by any ROM. We conclude that the present balanced modes allow to quasi-optimally recover the flow dynamics.

5.4. *Application: design of a full-state estimator*

We now give an example in the context of data assimilation showing how a ROM capturing the whole input and whole output spaces may be useful. For this, we consider upstream randomly distributed forcings. Such a situation mimics a true experiment where the upstream noise sources are unknown. In figure 14(*a*), we have

shown with small triangles the location of the considered forcings. Each triangle located at (x_f, y_f) refers to a momentum forcing $\boldsymbol{f} = (f, g)^{\mathrm{T}}$ of the form

$$[f(x, y), g(x, y)] = [\cos(\theta_f), \sin(\theta_f)] \exp[-((x - x_f)^2 + (y - y_f)^2)/\sigma_f^2] \tag{5.4}$$

where σ_f is the radius of each forcing and was set to a fixed value: $\sigma_f = 0.36$. The orientation θ_f of each forcing is a number comprised between $-\pi$ and π while x_f and y_f are chosen within $-1.25 \leqslant x_f \leqslant 1.25$ and $0 \leqslant y_f \leqslant 2$. At any time, two of these structures are present and the triplets (x_f, y_f, θ_f) randomly change every $\Delta t = 1$. These forcings are located near the beginning of the backward facing step, which is the sensitive region of the instability. Note that when a forcing is located in the lower left part of the forcing region, it is inactive since located outside the domain occupied by the fluid. Hence, there exists time intervals where the flow is not forced.

We now would like to estimate the velocity field of the resulting flow at every point and every time. The incoming flow is sensed thanks to a single shear-stress sensor located just downstream of the backward-facing step: $m_e = \int_{2.2}^{2.4} \partial_y u \, \mathrm{d}x$. A Kalman filter, whose gains are obtained by solving a Riccati equation, is used to build a dynamic observer. For this, a model comprising 1500 balanced modes obtained with $k = 40$ was considered and the noise was assumed to be Gaussian white in time and to force the flow only on the cross-stream momentum component ($\theta_n = \pi/2$), with a spatial structure of Gaussian shape located at $(x_n = -0.5, y_n = 1)$ and of radius $\sigma_n = 0.36$. We observe in figure 14(*a*) that this estimate (filled black half circle) is not very accurate when compared with the true noise environment. This has been done on purpose to show that the estimation process may be efficient even in the case where the noise environment is not accurately known. Finally, note that the sensor has been assumed to be perfect in the Kalman design, which means that the Kalman gains are obtained within the large-gain limit.

The simulation is launched at $t = 0$ and after a short transient, the flow sets in a permanent regime. At time $t = 100$, the estimator is switched-on: the measurement m_e is then fed into the Kalman filter, which in turn delivers at every time a vector $\boldsymbol{x}_r(t)$. From this, any information of the flow may be obtained at any point of the field. For example, in figure 14(*c*), we have represented the cross-stream component of the velocity m_D at point $(x_D = 12, y_D = 0.15)$. After a short transient, which corresponds to the time delay for a particle to travel from the shear sensor location (near $x = 2.2$) to the downstream station of interest here ($x_D = 12$), the estimated signal locks onto the real one given by the numerical simulation. In contrast, if we consider a sensor located upstream of sensor m_e, for example the cross-stream velocity component m_U at point $(x_U = 2, y_U = 0.89)$, then the performance is not as good. This can be observed in figure 14(*b*) where small discrepancies exist between the estimated and true signals. This stems from the fact that sensor m_e does not capture the upstream perturbation sufficiently early for the estimator to deliver an accurate signal at m_U. This issue has been discussed in Barbagallo *et al.* (2012) and is linked to the convective nature of the flow, where perturbations travel in the downstream direction. We have enclosed a movie (see movie.avi available at http://dx.doi.org/10.1017/jfm.2012.610) representing on the top (respectively bottom) figure the time-evolution of the streamwise component of the velocity field in the DNS (respectively the ROM). In the middle figure, we have shown the measurement m_e extracted from the DNS and which is the sole information that was given to the estimator to reconstruct the flow field. We observe that the Kalman filter, which is switched on at $t = 100$, is quickly very efficient.

It would be straightforward to add a controller to the presented setting. Since the ROM captures the whole output space, it is possible to target the overall perturbation energy. For this we could solve a Riccati equation with $M = T^{\dagger}T$ as the objective functional.

6. Conclusion

The two-dimensional incompressible flow over a rounded backward-facing step has been considered as a prototype of open flow subject to hydrodynamic instabilities. We investigated the linear dynamics of the flow excited by harmonic and stochastic forcing as well as the design of low-order models. The singular value decomposition of the resolvent has been performed in order to identify the optimal and suboptimal harmonic forcing/responses of the flow. These forcing/responses have been organized in branches of modes which clearly highlight two distinct dynamics. A first type of modes assesses the amplification and advection of perturbations as wave packets along the shear layer. In particular, it describes the Orr and Kelvin–Helmholtz instabilities. The second type of modes accounts for the convection of perturbations in the free stream, similarly to the continuous spectrum of flow configurations characterized by pure advection (Grosch & Salwen 1978). Once the dynamics is decomposed in the frequency domain, we showed how to use the optimal and suboptimal forcing/responses as a milestone to: (i) investigate the dynamics of the stochastically forced flow; and (ii) design accurate low-order models of the flow dynamics.

The potential of open flows to amplify external perturbations is typically assessed by scrutinizing their optimal perturbations and/or optimal forcing/respones. However, recurrent criticisms of these analyses concern the particular structure of these disturbances which can be unlikely to naturally emerge in real experiments as the noise does not excite these specific perturbations. An alternative analysis has been introduced in this paper by computing the leading EOFs and SOs. The techniques introduced here allow to both compute these modes and relate them to optimal forcing and responses. In particular, we have shown how to link the leading EOFs/SOs to the key instability mechanisms of the flow as well as specific frequency ranges. This work thus provides an additional tool to investigate the response of amplifier flows to external stochastic forcing.

The ROMs obtained by projection onto the leading EOFs, SOs and balanced modes recover the optimal perturbation of the system (the leading singular value of the time propagator) and the leading 40 optimal harmonic forcing/responses (the leading singular values of the resolvent). The original system of size $n = 170\,260$ has thus been reduced to models of size 1500 that accurately capture the map linking past forcing to future responses. One should expect that the balance between the ‘shear’ and ‘convective’ dynamics depends on the size of the computational domain. Actually, preliminary results performed on a bigger domain indicate that the free stream convective dynamics are more energetic while the shear layer ones remain almost the same. In such a case, a larger number of suboptimal forcing/responses would be required to capture the predominant input–output dynamics. We also conclude that designing accurate ROMs may be more challenging when considering much bigger computational domains.

The methodology introduced here is conceptually meant to capture the dynamics on a given frequency interval. In the case where the most energetic dynamics are predominantly driven by some known instability at a given frequency, as in the present study, it is possible to build ROMs that focus in this particular frequency

range by restricting the approximations of the Gramians to this range. For example, in view of closed-loop control, Barbagallo, Sipp & Schmid (2011) have shown that the ROM has to be accurate only in a small frequency band covering the dominant instability mechanisms to achieve efficient suppression of perturbations. Also, the ROMs designed in the present paper are not based on any specific input or output. They are meant to recover the original flow response from all the possible initial conditions or external excitations. This work thus yields a new and promising contribution to the design of ROMs for fluid flows. It may be a valuable asset in the design of Kalman filters for the estimation of the whole flow field in situations where the initial conditions or the upstream forcing are uncertain or varying. In the context of flow control, such models would allow to control the kinetic energy of the perturbations when the system is triggered by uncertain and varying in time forcing.

Supplementary movie

A supplementary movie is available at http://dx.doi.org/10.1017/jfm.2012.610.

REFERENCES

ÅKERVIK, E., EHRENSTEIN, U., GALLAIRE, F. & HENNINGSON, D. S. 2008 Global two-dimensional stability measures of the flat plate boundary-layer flow. *Eur. J. Mech.* B/*Fluids* **27** (5), 501–513.

ALIZARD, F., CHERUBINI, S. & ROBINET, J.-C. 2009 Sensitivity and optimal forcing response in separated boundary layer flows. *Phys. Fluids* **21**, 064108.

ALIZARD, F. & ROBINET, J.-C. 2007 Spatially convective global modes in a boundary layer. *Phys. Fluids* **19** (11), 114105.

BAGHERI, S., BRANDT, L. & HENNINGSON, D. S. 2009 Input–output analysis, model reduction and control of the flat-plate boundary layer. *J. Fluid Mech.* **620**, 263–298.

BARBAGALLO, A., DERGHAM, G., SIPP, D., SCHMID, P. J. & ROBINET, J.-C. 2012 Closed-loop control of unsteadiness over a rounded backward-facing step. *J. Fluid Mech.* **703**, 326–362.

BARBAGALLO, A., SIPP, D. & SCHMID, P. J. 2011 Input–output measures for model reduction and closed-loop control: application to global modes. *J. Fluid Mech.* **685**, 23–53.

BERKOOZ, G., HOLMES, P. & LUMLEY, J. L. 1993 The proper orthogonal decomposition in the analysis of turbulent flows. *Annu. Rev. Fluid Mech.* **25**, 539–575.

BLACKBURN, H. M., BARKLEY, D. & SHERWIN, S. J. 2008 Convective instability and transient growth in flow over a backward-facing step. *J. Fluid Mech.* **603**, 271–304.

BRANDT, L., SIPP, D., PRALITS, J. & MARQUET, O. 2011 Effect of base-flow variation in noise amplifiers: the flat-plate boundary layer. *J. Fluid Mech.* **687**, 503–528.

CHOMAZ, J.-M. 2005 Global stabilities in spatially developing flows: non-normality and nonlinearity. *Annu. Rev. Fluid Mech.* **37**, 357–392.

COSSU, C., PUJALS, G. & DEPARDON, S. 2009 Optimal transient growth and very large-scale structures in turbulent boundary layers. *J. Fluid Mech.* **619**, 79–94.

CROUCH, J. D., GARBARUK, A. & MAGIDOV, D. 2007 Predicting the onset of flow unsteadiness based on global instability. *J. Comp. Phys.* **224**, 924–940.

DERGHAM, G., SIPP, D. & ROBINET, J.-C. 2011 Accurate low dimensional models for deterministic fluid systems driven by uncertain forcing. *Phys. Fluids* **23** (9), 094101.

EHRENSTEIN, U. & GALLAIRE, F. 2005 On two-dimensional temporal modes in spatially evolving open flows. *J. Fluid Mech.* **536**, 209–218.

FARRELL, B. F. & IOANNOU, P. J. 1993*a* Stochastic forcing of the linearized Navier–Stokes equations. *Phys. Fluids* A **5** (11), 2600–2609.

FARRELL, B. F. & IOANNOU, P. J. 1993*b* Stochastic dynamics of baroclinic waves. *J. Atmos. Sci.* **50** (24), 4044–4057.

FARRELL, B. F. & IOANNOU, P. J. 1996 Generalized stability theory. Part I: autonomous operators. *J. Atmos. Sci.* **53** (14), 2025–2040.

FARRELL, B. F. & IOANNOU, P. J. 2001 Accurate low-dimensional approximation of the linear dynamics of fluid flow. *J. Atmos. Sci.* **58**, 2771–2789.

FONTANE, J., BRANCHER, P. & FABRE, D. 2008 Stochastic forcing of the Lamb–Oseen vortex. *J. Fluid Mech.* **613**, 233–254.

GROSCH, C. E. & SALWEN, H. 1978 The continuous spectrum of the Orr–Sommerfeld equation. Part 1. The spectrum and the eigenfunctions. *J. Fluid Mech.* **87**, 33–54.

HECHT, F., PIRONNEAU, O., HYARIC, A. LE & OHTSUKA, K. 2005 *Freefem++, the book*. UPMC-LJLL Press.

LAUB, A. J., HEATH, M. T., PAIGE, C. C. & WARD, R. C. 1987 Computation of system balancing transformations and other applications of simultaneous diagonalization algorithms. *IEEE Trans. Autom. Control* **32** (2), 115–122.

MARQUET, O., SIPP, D., CHOMAZ, J.-M. & JACQUIN, L. 2008 Amplifier and resonator dynamics of a low-Reynolds number recirculation bubble in a global framework. *J. Fluid Mech.* **605**, 429–443.

MONOKROUSOS, A., ÅKERVIK, E., BRANDT, L. & HENNINGSON, D. S. 2010 Global three-dimensional optimal disturbances in the blasius boundary-layer flow using time steppers. *J. Fluid Mech.* **650**, 181–214.

MOORE, B. 1981 Principal component analysis in linear systems: controllability, observability, and model reduction. *IEEE Trans. Autom. Control* **26**, 17–32.

NORTH, G. R. 1984 Empirical orthogonal functions and normal modes. *J. Atmos. Sci.* **41** (5), 879–887.

ROWLEY, C. W. 2005 Model reduction for fluids using balanced proper orthogonal decomposition. *Intl J. Bifurcation Chaos* **15**, 997–1013.

SIPP, D. & MARQUET, O. 2012 Characterization of noise amplifiers with global singular modes: the case of the leading-edge flat-plate boundary layer. *Theor. Comput. Fluid Dyn.* doi:10.1007/s00162-012-0265-y.

SIPP, D., MARQUET, O., MELIGA, P. & BARBAGALLO, A. 2010 Dynamics and control of global instabilities in open flows: a linearized approach. *Appl. Mech. Rev.* **63**, 030801.

TREFETHEN, L. N., TREFETHEN, A. E., REDDY, S. C. & DRISCOLL, T. A. 1993 Hydrodynamic stability without eigenvalues. *Science* **261**, 578–584.